POLITECNICO DI TORINO
Repository ISTITUZIONALE

Exploiting the potential of large eddy simulations (LES) for ducted fuel injection investigation in non-reacting conditions

Exploiting the potential of large eddy simulations (LES) for ducted fuel injection investigation in non-reacting conditions

C. Segatori [a], A. Piano [a,*], B. Peiretti Paradisi [a], A. Bianco [b], F. Millo [a]

[a] *Politecnico di Torino, Energy Department, Italy*
[b] *POWERTECH Engineering S.r.l., Italy*

ARTICLE INFO

ABSTRACT

The diesel combustion research is increasingly focused on ducted fuel injection (DFI), a promising concept to abate engine-out soot emissions in compression-ignition engines. A large set of experiments carried out in constant volume vessel and numerical simulations, at medium-low computational cost, showed that the duct adoption in front of the injector nozzle activates several soot mitigation mechanisms, leading to quasi-zero soot formation in several engine-like operating conditions. However, although the simplified CFD modelling so far played a crucial role for the preliminary understanding of DFI technology, a more accurate turbulence description approach, combined with a large set of numerical experiments for statistical purposes, is of paramount importance for a robust knowledge of the DFI physical behaviour.

In this context, the present work exploits the potential of large eddy simulations (LES) to analyse the non-reacting spray of DFI configuration compared with the unconstrained spray. For this purpose, a previously developed spray model, calibrated and validated in the RANS framework against an extensive amount of experimental data related to both free spray and DFI, has been employed. The tests have been carried out considering a single-hole injector in an optical accessible constant volume vessel, properly replicated in the simulation environment. This high-fidelity simulation model has been adapted for LES, firstly selecting the best grid settings, and then carrying out several numerical experiments for both spray configurations until achieving a satisfying statistical convergence. With this aim, the number of independent samples for the averaging procedure has been increased exploiting the axial symmetry characteristics of the present case study.

Thanks to this approach, a detailed description of the main DFI-enabled soot mitigation mechanisms has been achieved, shrinking the knowledge gap in the physical understanding of the impact of spray-duct interaction.

1. Introduction

The compression-ignition (CI) engine powered by diesel or biodiesel fuel is a leader technology in freight road transportation and shipping sectors, and will remain so for the next decades. In 2021, the European market share of new trucks was composed for 95.8 % by diesel trucks (ACEA, 2022) and, even in a net zero emissions by 2050 (NZE) scenario, more than 60 % of 2030 heavy trucks global sales will not adopt battery electric or fuel cell alternatives (IEA International Energy Agency, 2022). Assuming that the typical lifetime is about 9–17 years (Zhou et al., 2017), diesel trucks are expected to play a major role for many years to come. This argument is even more relevant for maritime shipping, whose NZE scenario forecasts an oil demand almost unvaried in the period 2021–2030 and approximately equal to 15 % of shipping fuel demand in 2050, since partly substituted by biofuels (i.e., up to 20 %) (IEA International Energy Agency, 2022). Therefore, assuming that

typical ship lifetime is between 20 and 35 years (IEA International Energy Agency, 2022), the reader can appreciate the importance of pushing nowadays research for the development of environmentally cleaner CI engine propulsion systems, minimizing direct and undirect pollutant emissions.

CI engines convert fuel energy in mechanical energy through the diesel combustion process (Heywood, 1988), which is well-known to produce high soot and nitrogen oxides (NOx) emissions, which are subsequently curtailed by very complex and expensive aftertreatment architectures before their release in atmosphere, in order to comply more and more stringent emissions standards (Villafuerte, 2022).

Ducted fuel injection (DFI) is one of the most promising strategies to curtail CI engine-out soot emissions by improving the conventional diesel combustion process enhancing the mixing between fuel and air inside the combustion chamber. The basic concept is the assembly of a coaxial small duct in front of the injector nozzle, positioned some distance downstream of it, to modify the entrainment and mixing processes of the diesel spray and ensure a lower fuel-to-air ratio in the autoignition zone, affecting the main driver of soot formation (Millo, Piano, Peiretti Paradisi, Postrioti, et al., 2021; Mueller et al., 2017). The capability to attenuate soot emissions by more than order of magnitude was demonstrated through constant-volume vessel (CVV) experiments (Gehmlich et al., 2018), and the suitability of its implementation in CI engine combustion chambers maintaining similar effectiveness was firstly shown through experiments in an optical engine equipped with a 2-holes injector (Nilsen et al., 2019). DFI impressive soot reduction potential can also be combined with high-dilution levels inside the combustion chamber via exhaust gas recirculation (EGR), a well-known extremely effective strategy to curtail NOx engine-out emissions (Pierpont et al., 1995). In fact, DFI was demonstrated to drastically change the behaviour of the so-called soot/NOx diagram traced with EGR sweeps, simultaneously reducing soot and NOx emissions, at least at low-load engine working points (Nilsen, Biles, et al., 2020). Finally, a very recent study provided evidence on the possibility to achieve future emissions regulations at an affordable aftertreatment cost and reduce at least 70 % of lifecycle carbon dioxide (CO_2) emissions, combining DFI with low-net-carbon fuels (Nyrenstedt et al., 2023). Based on the experimental data collected on a 1.72-liter single-cylinder optical engine working on a low-load (1 bar IMEPg) and a mid-load (10 bar IMEPg) working points, the researchers provided several solutions to meet heavy-duty future on-road and off-road emissions regulations for California, without using some of the aftertreatment systems. By combining DFI with renewable fuels featuring a significant oxygenation level, the off-road regulations could be satisfied without neither diesel particulate filter nor NOx aftertreatment system.

However, to ensure the success of this technology on the whole engine operating map and for different CI engine configurations, a deep understanding of fundamental working mechanisms is necessary. Several works moved in this direction, providing insights on some DFI physical principles based on experiments in test vessel (Li et al., 2019; Svensson & Martin, 2019) and on computational fluid dynamics (CFD) simulations (Fitzgerald et al., 2018; Lucchini et al., 2022; Millo, Piano, Peiretti Paradisi, Postrioti, et al., 2021; Millo, Piano, Peiretti Paradisi, Segatori, et al., 2021; Nilsen, Yraguen, et al., 2020) in both non-reacting and reacting conditions. In particular, the CFD resulted as a very valuable tool for DFI exploration, overcoming the non-intrusiveness limits of experimental investigation and enabling the observation of physical phenomena occurring inside and close to the duct, such as air entrainment and turbulent mixing. Nevertheless, all the above-mentioned research works relied on the modelling of turbulence instead of directly solving it, namely using the low-cost Reynolds-averaged Navier–Stokes (RANS) turbulence models instead of directly solving at least the largest turbulent length scales, through a large eddy simulation (LES) approach. It is well-known how, for highly turbulent case studies, a LES capable to satisfy the quality criteria guarantees more accurate and reliable results with respect to the corresponding RANS simulation,

with the drawback of a much higher computational cost (Celik et al., 2001; Pope, 2000). Therefore, considering that the turbulence plays a dominant role in DFI mixing process and that typical RANS turbulence models loose of generality when not trivial flow/wall interactions are present, like in DFI case, the usage of LES increases in importance for a robust and detailed knowledge on the topic.

Some researchers performed LES aiming at investigating DFI technology. (Chen et al., 2023; Zhang et al., 2021) carried out a single LES realization of DFI under non-vaporizing conditions using injector nozzles diameter of 0.120 mm and 0.140 mm, respectively, while (Feng et al., 2023; Guo et al., 2023; Ong et al., 2022) investigated DFI under ECN Spray A (Skeen et al., 2016) reacting conditions (i.e., 0.090 mm nozzle diameter).

Despite several insights on the DFI entrainment and mixing processes have been provided by them, according to the Authors' opinion, no study has exploited the full potential of this turbulence description approach for several reasons. Firstly, the adopted computational grids were relatively coarse making most of these analyses fall in the very large eddy simulation (VLES) field (Speziale, 1997), reducing the reliability of the results. Secondly, LES was not combined with statistics, which is suggested due to the run-to-run variability of this kind of approach, thus the single-realization results lack of generality (Hanjalic, 2005). Thirdly and subsequently, a detailed analysis of the ducted spray turbulent characteristics was not performed and the DFI-enabled resolved turbulent kinetic energy (TKE) field was not compared with the free spray one. Furthermore, from an applicative point of view, the present study uses a single-hole injector featuring a nozzle diameter equal to 0.180 mm, similar to ECN Spray D, thus more relevant to heavy duty applications (Chung et al., 2020) with respect to previous cited studies.

Therefore, the aim of this work is to exploit the potential of LES combined with statistical analysis to explore the non-reacting spray of DFI configuration compared with the unconstrained spray towards its full comprehension, under conditions which are relevant to heavy duty CI engines. For this purpose, a highly refined grid was adopted to ensure a high-quality LES (Pope, 2004) together with a statistically significant sample size for both spray configurations. Then, a detailed analysis of the ducted spray turbulent characteristics was performed, improving its understanding to support DFI development and optimization.

2. Materials and methods

2.1. Case study

The experimental case study considered for the herein 3-dimensional (3D) CFD study is a cylindrical 1.5L CVV, equipped with a co-axial prototype single-hole common rail injector featuring a nozzle diameter equal to 0.180 mm and injecting standard diesel fuel. The analysis is conducted under the non-reacting operating conditions reported in Table 1, falling into the CI engine typical operating range. Furthermore, the injection characteristics in terms of pressure, duration and mass are reported as well.

For the DFI configuration, the same duct geometry already employed in other works (Fitzgerald et al., 2018; Li et al., 2019; Millo, Piano, Peiretti Paradisi, Postrioti, et al., 2021; Millo, Piano, Peiretti Paradisi, Segatori, et al., 2021) was considered to consistently compare the main findings. This duct features an inner diameter (D) of 2 mm, a length (L)

Table 1
– Case study non-reacting operating conditions.

Oxygen concentration	0 %
Vessel pressure	20 bar
Vessel temperature	773 K
Rail pressure	1200 bar
Injection duration	1.5 ms
Injected mass	11.85 mg

of 14 mm, a stand-off distance (G) of 2 mm, and a wall thickness of 0.5 mm. It is named D2L14G2 according to the herein used convention (D<diameter>L<length>G<stand-off distance>).

This case study is taken from the experiments and RANS simulations in (Millo, Piano, Peiretti Paradisi, Postrioti, et al., 2021; Millo, Piano, Peiretti Paradisi, Segatori, et al., 2021).

2.2. 3D-CFD setup

2.2.1. Overview

The numerical simulations were carried out on the commercially available software CONVERGE CFD 3.0.14 (Richards et al., 2022). The post-processing of the 3D results was conducted on MATLAB R2021a (Mathworks, 2021).

Wall-type fixed-temperature (equal to the vessel temperature) boundary conditions were set for the whole CVV as well as the duct wall. The heat exchange was taken into account through the O'Rourke and Amsden model (Amsden & Findley, 1997). The domain was initialized with an almost quiescent flow based on the experimental test boundary conditions. Considering a start of injection occurring 0.3 ms later than the start of the simulation, and the injection event simulated for 0.5 ms, the total simulation duration was set equal to 0.8 ms. This time window is sufficient for the spray to cover the whole length of the experimental optical access window (i.e., approx. 50 mm in the spray axis direction), thus achieving pseudo-stationary conditions in the spatial window of interest.

Concerning the numerical aspects, the flow field was solved by means of a finite volume method employing a second-order central difference scheme for spatial discretization. The pressure implicit with splitting of operators (PISO) algorithm (Issa, 1986) coupled with the Rhie–Chow scheme for pressure-velocity coupling (Rhie & Chow, 1983) was adopted to solve the Navier–Stokes equations. The second-order, numerically stable, Crank–Nicolson method was adopted for the temporal discretization. A variable time-step was set, dynamically determined by the Courant–Friedrichs–Lewy (CFL) limits, to minimize the runtime maintaining the solution accuracy.

2.2.2. Spray model

The same spray model employed in previous works (Millo, Piano, Peiretti Paradisi, Postrioti, et al., 2021; Millo, Piano, Peiretti Paradisi, Segatori, et al., 2021; Millo, Segatori, et al., 2021), which modelled turbulence according to the RANS approach, was herein exploited. The underlying hypothesis is that the turbulence modelling approach, moving from RANS to LES, does not affect the liquid-related results to such an extent as to involve a modification of the spray sub-models selection and calibration. This hypothesis has been carefully verified, as reported in the model validation section.

The Lagrangian particle tracking approach was adopted for the spray modelling, injecting parcels with a diameter equal to the effective nozzle hole diameter according the blob injection model (Reitz & Diwakar, 1987) and with a near spray cone angle accurately set according to the experimental spray imaging acquisitions. The number of injected parcels was chosen to guarantee a good balance between liquid and gas phase in each cell, avoiding overestimation of the penetration due to high liquid volume fraction (Senecal, Pomraning, Richards, et al., 2014). This number was changed according to the minimum grid size. The primary and secondary breakup processes were described according to the KH-RT model without breakup length (Reitz & Bracco, 1986). The collision model was neglected for the present case study. The drop drag phenomenon was modelled as dynamic drop drag, in order to take into account the deformation of each droplet due to aerodynamic resistance (Liu et al., 1993). Concerning the fuel physical characteristics, the liquid phase was represented by Diesel #2 liquid fuel, while the normal-heptane (N-C7H16) was selected as single species for the gas phase. The evaporation process occurred according to the Frossling model, considering also the boiling process (Amsden et al., 1989). The

rebound/slide model (Gonzalez et al., 1991; Naber & Reitz, 1988) was employed as spray / wall interaction model, particularly important for the DFI configuration. Additional comments regarding this selection can be found in Appendix A.

The spray sub-models were selected, calibrated and validated through an extensive comparison with the experimental data for several combinations of rail pressure, vessel temperature and vessel pressure for both free spray and DFI configurations. High predictivity was achieved by the RANS model in the whole operating range. Further details on the calibration and validation processes in the RANS framework can be found in (Millo, Piano, Peiretti Paradisi, Postrioti, et al., 2021).

2.2.3. Turbulence model and wall treatment

The turbulence was described by means of the LES approach, directly resolving the largest turbulent eddies from the Navier–Stokes equations, while modelling the smallest ones, more isotropic and less case dependent. A spatial filter, defined through the minimum grid size, establishes the passage from solved to unsolved turbulent structures (i.e., sub-grid scale).

The sub-grid scale (SGS) was modelled through the one-equation dynamic structure model (Pomraning & Rutland, 2002). This non-viscosity model, on one hand, does not require *a priori* knowledge of the flow coefficients that, instead, are dynamically determined as a function of time and space from the resolved field; on the other hand, provides a reliable estimation of the SGS TKE (Senecal et al., 2013).

Considering the present case study, the whole optical window was resolved through LES for the free spray. Instead, for the DFI configuration, the need to guarantee a physical solution at the duct wall provided additional complexity to the simulation setup. Two options were available for this purpose: LES with near wall resolution (LES-NWR) approach or LES with near wall modelling (LES-NWM) approach (Pope, 2000). LES-NWR, meaning directly resolving the boundary layer, requires a non-dimensional wall distance ($y+$) lower than 1 together with an almost isotropic mesh (i.e., flow field must be resolved in the streamwise and spanwise direction (Martínez et al., 2015)). However, LES-NWR for this case study would lead to a prohibitive number of cells, increasing as a power of Reynold number (Chapman, 1979), and thus a computational cost similar to direct numerical simulation (DNS) (Pope, 2004) due to the high Reynolds number in the duct (Li et al., 2019; Millo, Piano, Peiretti Paradisi, Postrioti, et al., 2021). Therefore, LES-NWM approach (Piomelli, 2008) has been employed, meaning applying a wall function at the duct wall, adopting a first cell sufficiently large to include the whole viscous wall region. In particular, the Werner and Wengle wall function (Werner, H., Wengle, 1991) was used and care was taken for its correct application, maintaining the $y+$ in the suggested range ($30 < y+ < 300$), as dealt with in the grid sensitivity analysis.

The application of a RANS-LES hybrid mode, like detached eddy simulation (DES) (Spalart, 2009), might have been one of the options, allowing the description of the boundary layer, not requiring a high grid resolution in the direction tangential to the wall. However, it is worth noting that DES is mainly thought for aerodynamic highly detached external flows while features some issues when deals with internal flows (Mockett et al., 2012; Mockett & Thiele, 2007; Slimon, 2003; Travin et al., 2006), like the in-duct region of DFI. For this reason, it has been discarded.

2.2.4. Grid settings

The CVV was entirely meshed with a cartesian grid featuring a base grid of 2 mm and processing the cells at the wall according to the patented cut-cell technique in (Senecal et al., 2007). Starting from the base grid size, the mesh was gradually refined towards the spray main area by adopting several fixed refinement regions, according to the rule in Eq. (1):

$$dx_{ref} = \frac{dx_{base}}{2^f} \qquad (1)$$

where f, the refinement factor, is an integer.

The fixed refinement regions are illustrated in Fig. 1, together with the associated longitudinal dimension and refinement factor value.

As can be seen, each refinement was parametrically defined as a function of the same variable "r" (with $r > 2$), whose final value has been determined according to a grid sensitivity analysis, illustrated later in the text. In particular, three fixed refinement regions were employed: a first cylinder covering the whole optical access window; a second cylinder covering the near-spray region (i.e., twice the axial duct occupancy), and the volume inside the duct. The latter was not used for the free spray configuration. Moreover, the adaptive mesh refinement (AMR) based on local velocity and temperature gradients was adopted to achieve the maximum refinement (i.e., $f = r$) where required in the whole domain, without unnecessary increment of the computational cost.

As far as the DFI configuration is concerned, since the analysis is based on the LES-NWM approach, the y+ must be maintained in the optimal range for correct wall function application. For this purpose, a 1-layer inlaid mesh was extruded from the duct inner wall to enable an additional degree of freedom in structuring the grid. This choice was pursued for two main reasons: on one hand, the inlaid mesh is unrelated to the cartesian grid, thus the grid size at the duct wall can be optimized flexibly with respect to a fixed cartesian refinement; on the other hand, the extrusion from the wall avoids cell shape variation due to the cartesian cut-cell technique, ensuring cells homogeneity in the circumferential direction. A 62.5 μm inlaid mesh was adopted, approximately equal in radial, axial and circumferential direction to guarantee an almost isotropic mesh. This 1-layer cell size, on the one hand, maintained the solution in the optimal log-law region satisfying the relation $30 < y+ < 300$ for the whole duct inner wall, on the other hand, limited to a reasonable amount the number of cartesian/inlaid cell neighbours, thus ensuring a high mesh quality.

According to the grid settings and constraints defined above, a grid sensitivity analysis was performed aiming at figuring out the most appropriate grid size which solved at least 80 % of the turbulent structures in the whole domain, as suggested by (Pope, 2000, 2004) for a high-quality LES. In particular, the r parameter was swept from 4 to 6 keeping the 1-layer inlaid mesh equal, leading to minimum grid sizes sweeping from 125 μm to 31.25 μm for both free spray and DFI configurations. However, only the results of the grid sensitivity analysis applied to the DFI case are presented in this work. Please refer to (Segatori et al., 2023) for details on the grid sensitivity analysis applied
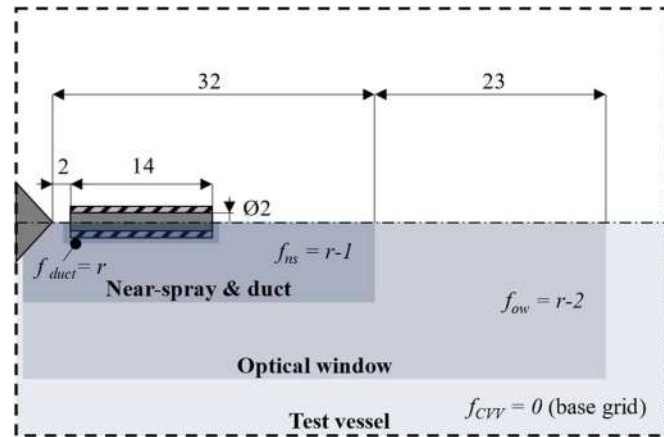
to the free spray case, considering that the final simulation setup adopted the same r parameter for both free spray and DFI configurations. It is worth noting that, when LES is adopted, the best solution is approached as the grid size is reduced, since the spatial filter is gradually shifted towards smaller turbulent structures, increasing the resolved portion of the turbulent energy spectrum while reducing the influence of the SGS modelled part. Hence, in other words, the purpose of the grid sensitivity analysis was establishing the smallest resolved turbulent scales and, thus, the quality of the LES resolution as well as the computational cost required for the subsequent physical investigation. The maximum number of cells, the minimum time-step, the number of injected parcels and the corresponding core hours on the available high-power computing (HPC) resources are reported in Table 2 for each step of the grid sensitivity analysis considering a single DFI simulation.

As the grid is refined, the computational cost drastically increases even for a single simulation. This is due to the higher number of cells, the reduction of the minimum time-step to respect the CFL restrictions and the higher number of injected parcels to avoid any overestimation of the penetration related to an excessive liquid fraction in the computational cells. In this context, it is important to stress the fact that several realizations are needed for LES statistics, each one costing the just mentioned computational resources.

Concerning the resolved flow field associated with each minimum grid size, in Fig. 2, the ensemble-averaged equivalence ratio (ϕ) and velocity magnitude fields on a semi-slice passing for the spray axis are reported for DFI at 0.3 ms aSOI considering each minimum grid size. The injector nozzle is located at r=0 mm, Z=0 mm. The ensemble average among 20 different samples was considered, using the ensemble average method analysed in detail later in a specific paragraph.

As can be seen, large variations of the ensemble-averaged solution are present moving from the 125 μm grid to the 62.5 μm grid, and significant variations are still present for the further grid refinement up to 31.25 μm. In general, a reduction of the equivalence ratio value throughout the ducted spray plume is observable as the grid is refined, especially looking at the spray tip and at the rich pockets close to the wall at the duct exit. In particular, the rich pockets at the duct exit change in extension, since the flow detachment is predicted as more retarded if the grid is not sufficiently refined. This affects also the enlargement of the spray cone angle at the duct outlet, which is higher as the grid is refined. Furthermore, the penetration is progressively reduced as well as the ducted-spray tip shape changes towards a mushroom-shaped head, typical of the DFI non-reacting spray (Li et al., 2020). Finally, the refinement of the grid allows also a better prediction of the velocity magnitude values inside the duct. Therefore, in this case study, the adoption of a minimum grid size higher than 31.25 μm would lead to a not properly captured DFI behaviour and even a probable underestimation of its effectiveness in terms of mixing.

Finally, an additional check was carried out to determine the best grid settings: the turbulence resolution index (TRI) (Segatori et al., 2023) was evaluated to indicate the local value of the ratio between the resolved TKE and the total TKE (i.e., resolved plus sub-grid scale TKE), as in Eq. (2):

$$TRI(X, Y, Z) = \frac{TKE_{resolved}}{TKE_{total}} = \frac{TKE_{resolved}}{TKE_{resolved} + TKE_{SGS}} \qquad (2)$$

Fig. 1. – Fixed refinement regions with the associated refinement factors (f) and dimensions for the DFI configuration. Main duct geometrical characteristics also provided.

Table 2
– Computational details for a single DFI simulation as a function of the minimum grid size. Processors: x86 Intel Xeon Platinum 8276-8276L (2.4 GHz).

dx_{min}	Max N° cells	Min time-step	N° injected parcels	Core hours
125 μm ($r = 4$)	≈ 2M	1.4e-07 s	2M	≈ 0.1k
62.5 μm ($r = 5$)	≈ 13M	5.8e-08 s	8M	≈ 1.1k
31.25 μm ($r = 6$)	≈ 87M	3.0e-08 s	21M	≈ 29.8k
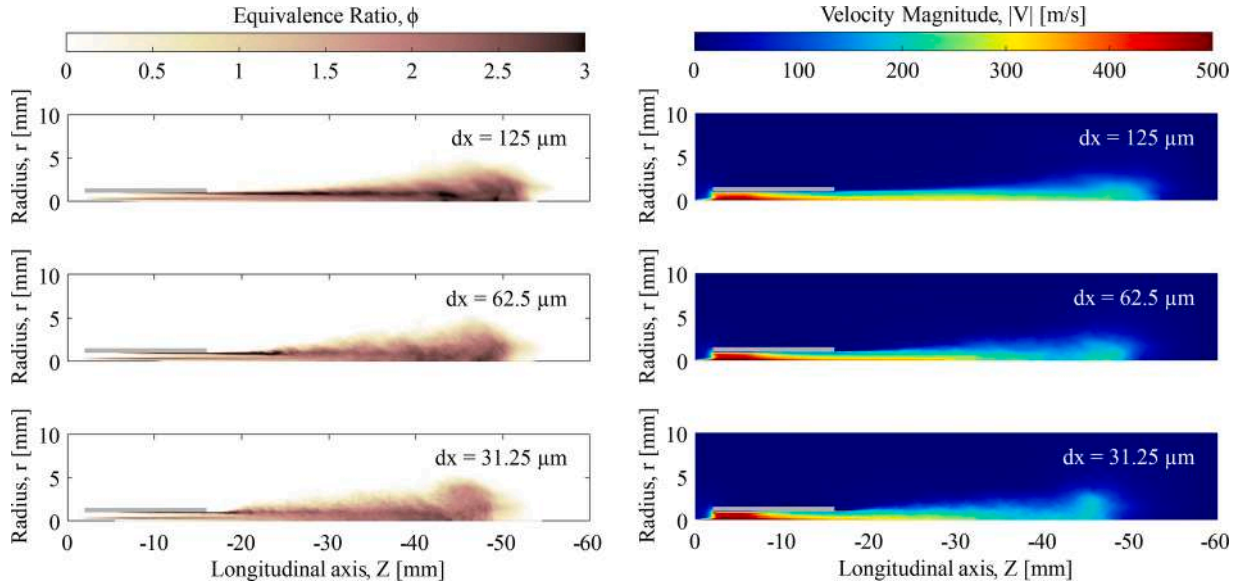
Fig. 2. – Sensitivity analysis to the grid size for the DFI configuration: ensemble-averaged equivalence ratio (left) and velocity magnitude (right) distributions of the ensemble average among 20 samples on a semi-slice passing for the spray axis at 0.3 ms aSOI as a function of the minimum grid size.

As abovementioned, a minimum amount of resolved turbulent structures equal to 80 % was targeted to guarantee a high-quality LES (Pope, 2000, 2004), therefore a minimum value of 0.8 is imposed for the TRI, where 0 characterizes a RANS simulation (completely modelled turbulence) and 1 characterizes a DNS (completely resolved turbulence). For the resolved TKE computation, the root mean square (RMS) of the velocity components fluctuations with respect to the average components were evaluated considering, as above, the ensemble average among 20 different samples. In Fig. 3, the TRI fields for the DFI configuration at 0.3 ms aSOI are depicted on a semi-slice passing for the spray axis for each considered grid size. As above, 20 samples were considered for the ensemble average and resolved TKE computation. In
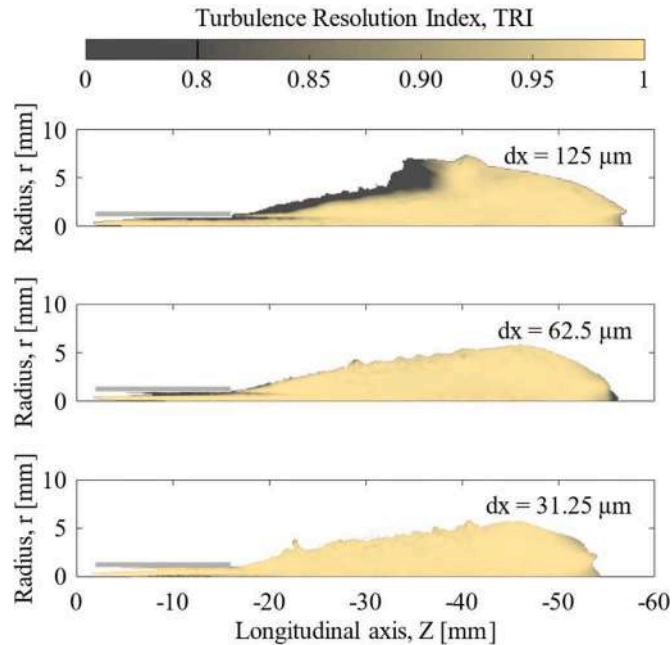
order to avoid areas at a very low turbulence level, only the cells featuring $\phi > 0.01$ are represented to define the domain of interest.

According to the adopted colour scale, the saturated grey highlights the locations not satisfying the imposed minimum resolution requirements, while the light-yellow highlights the well-resolved locations. As can be seen, the 125 μm grid features a poor resolution both inside the duct and along the spray periphery. The latter deficiencies seem overcame by the 62.5 μm grid, sufficiently resolving most of the spray plume, but a poor resolution is still present inside the duct and immediately after the duct exit. This is consistent with the retarded rich pockets' breakage at the duct outlet, previously described (Fig. 2) for this intermediated grid size. Finally, the 31.25 μm grid resolves the whole domain of interest with a TRI higher than 0.8.

Therefore, these results provide extensive evidence that the 31.25 μm grid is necessary for an accurate physical analysis of the DFI configuration under the considered operating conditions. According to this, the most refined $r = 6$ was chosen as final value, accepting to deal with a dramatically larger computational cost, affecting both runtime and postprocessing time, associated with the final grid configuration. This huge computational cost was partially reduced by means of the ensemble average methodology presented in (Segatori et al., 2023), enabling a lower number of simulations keeping constant the number of available samples for the average.

2.3. Ensemble averaging process

A total number of samples equal to 20 was considered for both free spray and DFI to carry out the LES statistical analysis. This value can be considered enough to reach a sufficiently stable average in non-reacting conditions (Hu et al., 2015; Segatori et al., 2023; Senecal, Pomraning, Xue, et al., 2014), in line with scope of the work. The variability among different simulations was triggered through variation of the random seed parameter used in the spray sub-models, as executed by Senecal et al. (2013) to introduce perturbations and mimic the spray-to-spray variability characterizing experimental injections.

The huge computational cost, associated with the chosen highly refined grid, was curtailed by means of the so-called *Multi-Slice* approach. It consists in exploiting the axial-symmetry characteristics of the case study by dividing a single simulation outcome in several semi-slice passing for the spray axis and considering each of them as a different sample for the average. This method is schematized in Fig. 4 in

Fig. 3. – Sensitivity analysis to the grid size for the DFI configuration: turbulence resolution index distribution of the ensemble average among 20 samples on a semi-slice passing for the spray axis at 0.3 ms aSOI as a function of the minimum grid size.
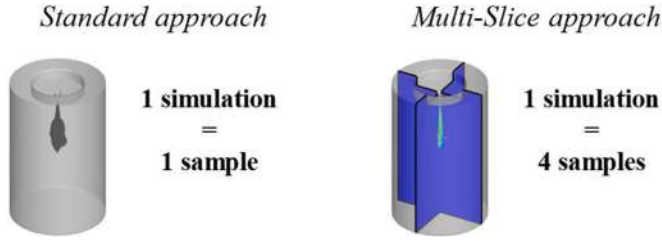
Fig. 4. – Sketch of the multi-slice (4 slices) ensemble average approach compared with the standard approach.

comparison with the standard approach.

Keeping constant the required total number of samples, this methodology allows reducing the number of simulations by a factor equal to the number of semi-slices considered for each simulation, with the drawback of limiting results to a 2D representation. This runtime saving ensemble average approach is occasionally proposed in the literature on LES spray simulations (Farrace et al., 2015; Pitsch & Steiner, 2000) and the reliability of the final outcome has been demonstrated for both free and DFI sprays in (Segatori et al., 2023), where a number of slices per simulation equal to 4 guaranteed statistical independence and allowed avoiding grid-induced asymmetries due to the usage of the cartesian grid. The same criteria were applied in this work, thus, only 5 simulations for each configuration were necessary to achieve the targeted total number of samples (i.e., 20). For instance, about 447k core hours have been saved just for the DFI configuration, according to the data in Table 2.

3. 3D-CFD model validation

In order to provide robustness to the present analysis, a comparison of the liquid spray outcome obtained through experiments and LES is herein reported. For this purpose, a methodology was developed for consistent comparison of experimental optical data and 3D-CFD liquid parcels distribution. Details regarding this methodology are reported in Appendix B.

In Fig. 5, the liquid spray contours are reported for both free spray and DFI configurations at four different time instants. The spray contours are associated to a single randomly chosen realization for both experiments and LES.

Focusing on the free spray configuration (Fig. 5 - left), at each time instant the experimental trace (black pixels) is correctly captured from an overall perspective by the LES (red pixels). In particular, the developed cone angle is almost overlapped and the penetration is very similar between the traces. Furthermore, a similar shape of the spray tip is predicted. Moving to the DFI configuration (Fig. 5 - right), good predictions are obtained in terms of overall behaviour. In this case, the LES (blue pixels) slightly underestimates the spray dispersion angle downstream of the duct, while accurately captures the penetration and the spray tip shape.

4. Results and discussion: free spray vs DFI

First of all, the need for statistical analysis with LES is motivated by showing the run-to-run variability for both free spray and DFI. In Fig. 6, the ϕ fields on a plane passing for the spray axis at 0.5 ms aSOI are depicted for both free spray and DFI for 5 randomly chosen realizations
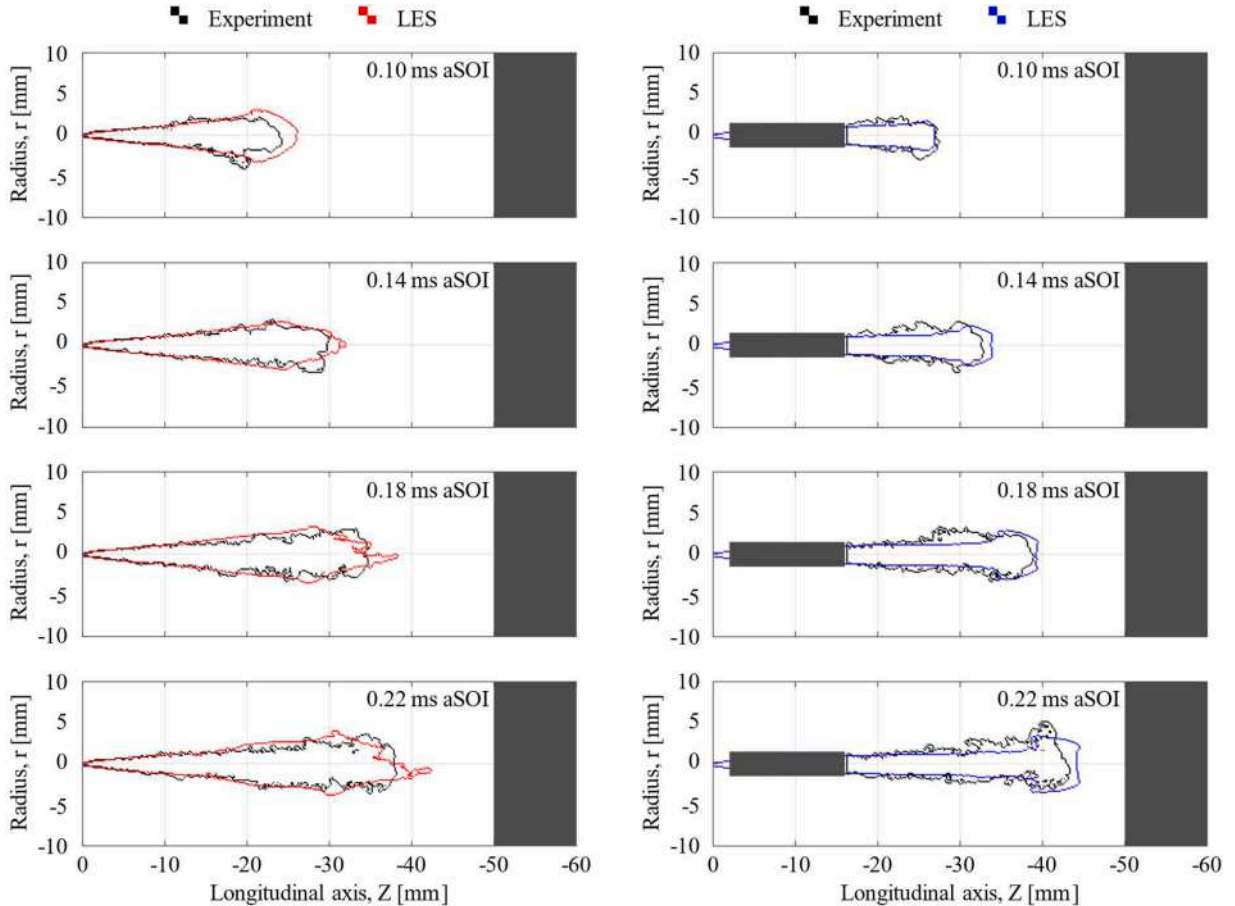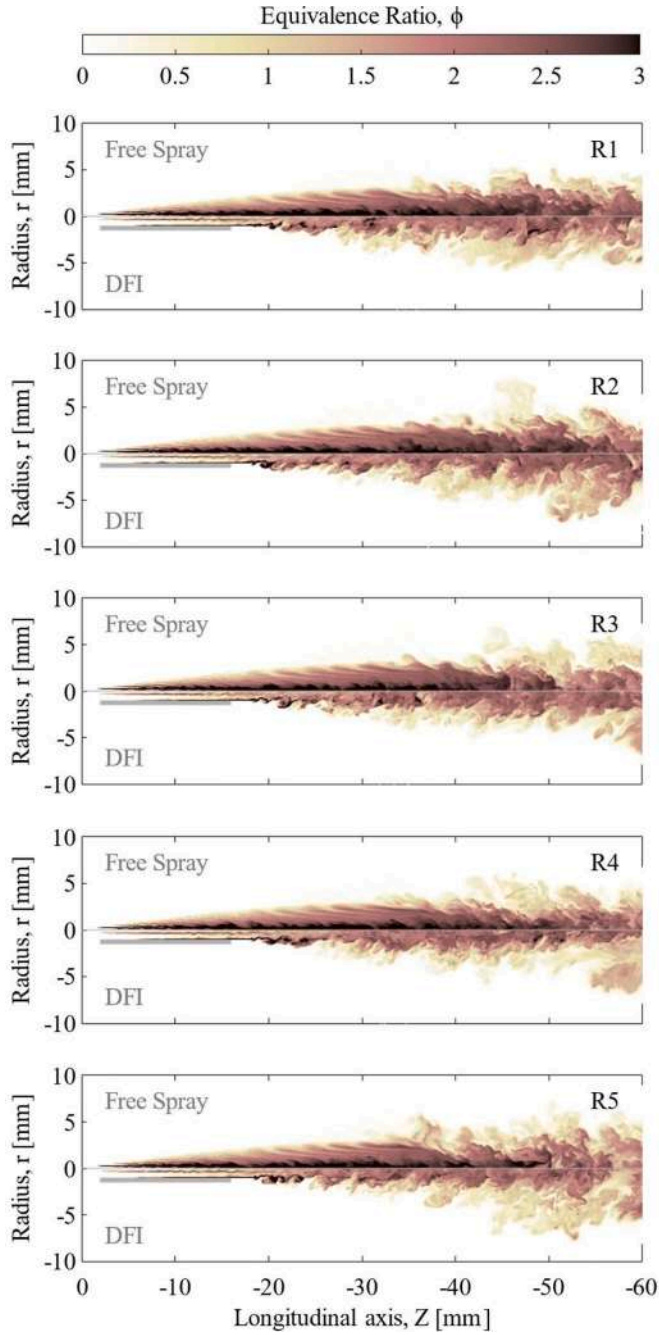

Fig. 5. – Liquid spray contours extracted from experimental pictures (black) and LES simulations (red / blue) for both free spray (left) and DFI (right) configurations at four different time instants. Results obtained from a single randomly chosen realization for both experiment and LES.
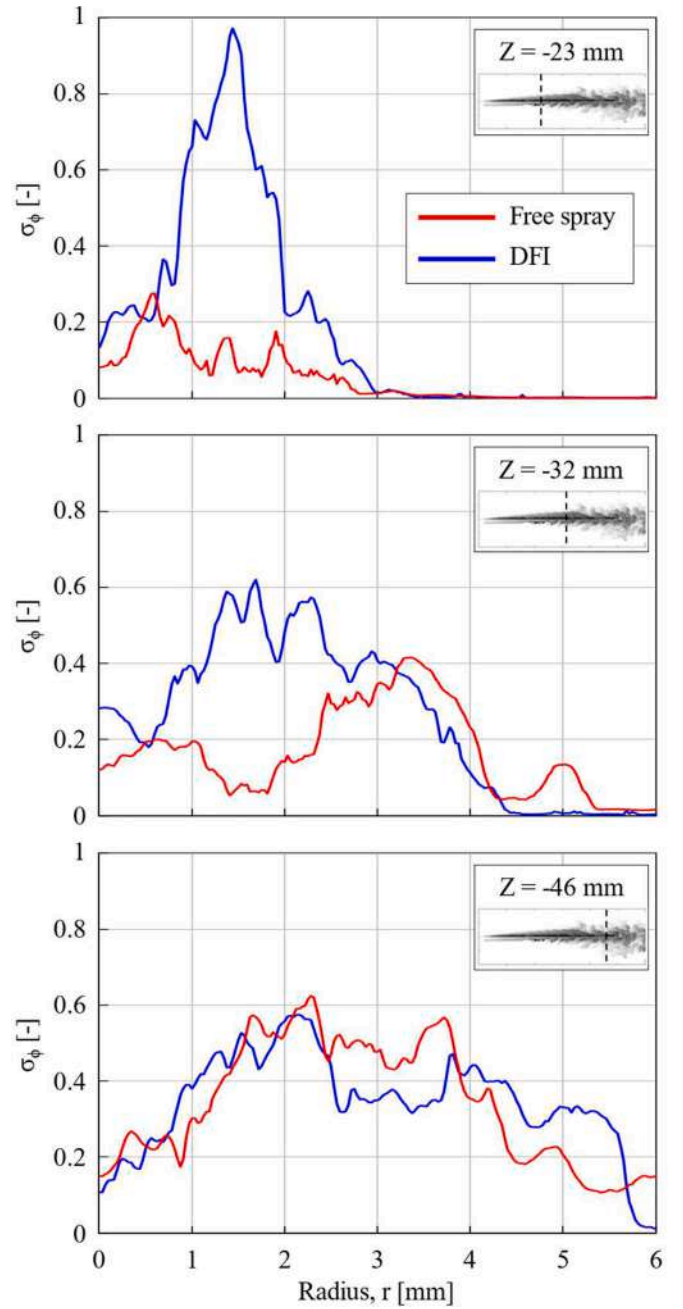
Fig. 6. – Equivalence ratio fields on a semi-slice passing for the spray axis at 0.5 ms aSOI for both free spray (top side) and DFI (bottom side) for five different randomly-chosen realizations (R).

Fig. 7. – Standard deviation of the equivalence ratio as a function of the spray radius at 0.5 ms aSOI for both free spray (red) and DFI (blue) at three different axial positions: $Z = -23$ mm (top); $Z = -32$ mm (middle); $Z = -46$ mm (bottom).

(R). The free spray is represented on the top side of each spray, while the DFI on the bottom side.

Although from an overall point of view the results do not undergo a dramatic change from realization to realization, a large variability is present with a pointwise approach starting from the Z at which vortices start to form. This location is advanced in space for the DFI, leading in general to a larger variability with respect to the free spray. For instance, the length of the rich pocket close to the wall at the duct exit varies in the range 20–24 mm, leading to significant differences in the downstream ϕ values.

To analyse these differences in variability from a more quantitative perspective, in Fig. 7, the standard deviation of the equivalence ratio (σ_ϕ) as a function of the spray radius is reported for both free spray and

DFI at three different axial positions.

High standard deviation values are reached for the DFI configuration at the more advanced location, close to the duct exit, associated to the variability of the rich pockets previously mentioned, while low values are present for the free spray. A higher σ_ϕ is then maintained at the intermediate location, manifesting a higher relevance of the turbulence when the duct is present. Only for the farther location from the injector nozzle the free spray σ_ϕ becomes comparable to the DFI one.

In Fig. 8, the ϕ behaviour as a function of the spray radius is reported for both free spray and DFI at three different axial positions. In particular, a comparison across the entire dataset (i.e., 20 realizations per configuration) is reported together with the ensemble average behaviour. The free spray is on the right side, the DFI on the left side.

Focusing on the $Z = -23$ mm location (Fig. 8 - top), it can be seen a

Fig. 8. – Equivalence ratio as a function of the spray radius at 0.5 ms aSOI for both free spray (right side) and DFI (left side) at three different axial positions: 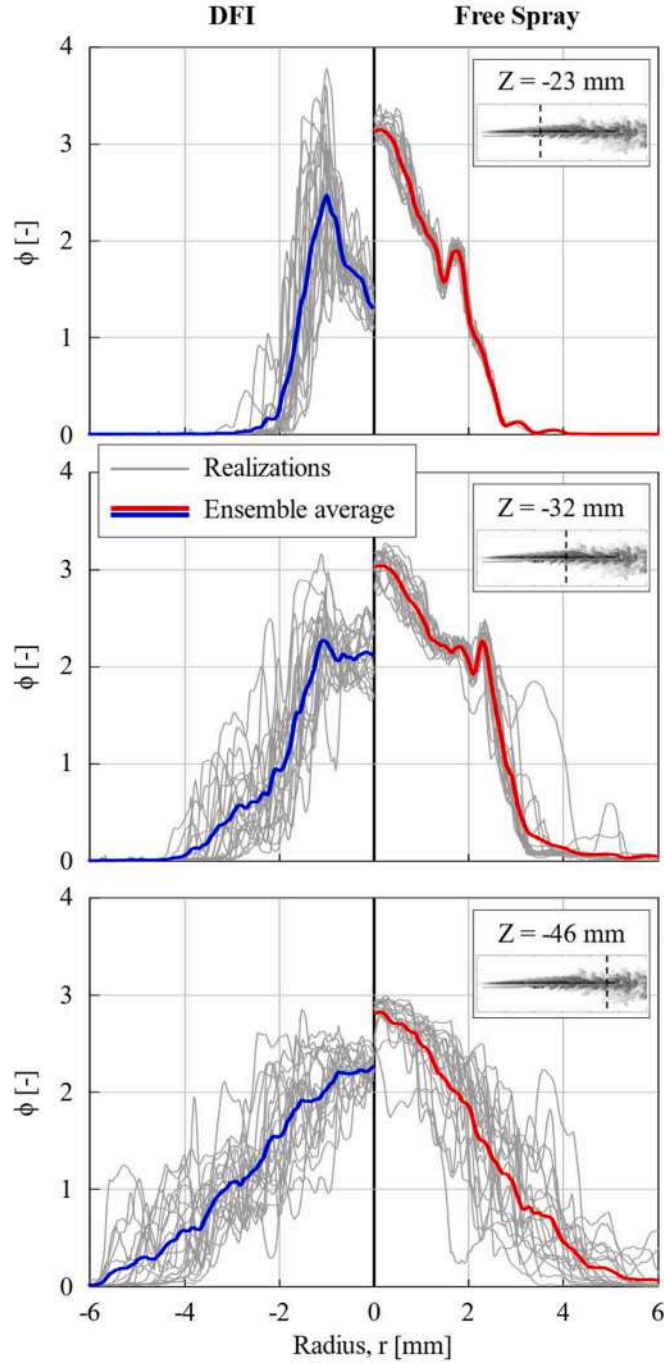Z = -23 mm (top); Z = -32 mm (middle); Z = -46 mm (bottom). Comparison between the ensemble averages (red and blue) and 20 different realizations (grey).

peak for the DFI at r = 1 mm, manifesting the presence of the above-mentioned rich pocket. However, the magnitude of this peak is remarkably affected by run-to-run variability, falling in a ϕ window greater than 2. On the contrary, the maximum ϕ value is in the centre-line for the free spray and shows a window of variability lower than 0.5. Moving to the Z = -32 mm location (Fig. 8 - middle), the dispersion starts to increase for the free spray, especially towards the periphery, but the ensemble average is still representative of most of the realizations. For the DFI, the rich peak is smoothened and a homogenization process is evident within the centre of the spray, showing almost constant ϕ value

for a radius lower than 1 mm. Concerning the variability, a large dispersion is still present in the centre and becomes larger towards the periphery. Looking at Z = -46 mm (Fig. 8 - bottom) location, the free spray features a variability which is comparable to the DFI. Focusing on the average curves, a similar bell-shape distribution is reached by both configurations, despite the values are significantly different. It is noteworthy that the ϕ average values do not show important reduction along the axis because the spray is still undertaking the evaporation process, since the liquid fraction is present at least in the first 50 mm under these injection conditions (Millo, Piano, Peiretti Paradisi, Postrioti, et al., 2021). Finally, from a general view, comparing the average curves for DFI (blue) and free spray (red), an initial insight into the duct-enabled mixing effectiveness can be gained, since the DFI shows significantly lower ϕ average values at each considered axial distance. In particular, ϕ values lower than or very close to 2 are achieved by the DFI average curves, approaching mixture conditions necessary for a soot-free diesel combustion (so-called leaner lifted-flame combustion regime (Polonowski et al., 2012)).

In order to visualize and compare the average behaviour on the whole domain of interest, the ensemble-averaged ϕ fields on a plane passing for the spray axis in both transient (0.3 ms aSOI) and pseudo-stationary (0.5 ms aSOI) phases are depicted in Fig. 9 for both free spray and DFI.

First of all, the main differences in terms of spray shape between free spray and DFI can be clearly detected: the typical mushroom-shaped head for the DFI spray tip during the transient phase (Fig. 9 - top) (Li et al., 2020), as well the larger spray area downstream of the duct due to higher spray dispersion angle during the pseudo-stationary phase (Fig. 9 - bottom) (Li et al., 2019).

Focusing on the ϕ values, the average rich zone, highlighted with the saturated black colour, is completely different in terms of position, longitudinal extension and radial extension between free spray and DFI. In fact, the rich core in the centreline for the free spray is broken more than 20 mm later than the DFI pocket, located just downstream of the duct at r = 1 mm. Furthermore, the spray core is almost lean for DFI, as already reported in Fig. 8. Therefore, a leaner and more homogeneous distribution is present for DFI, at least starting from about 20 mm axial distance.
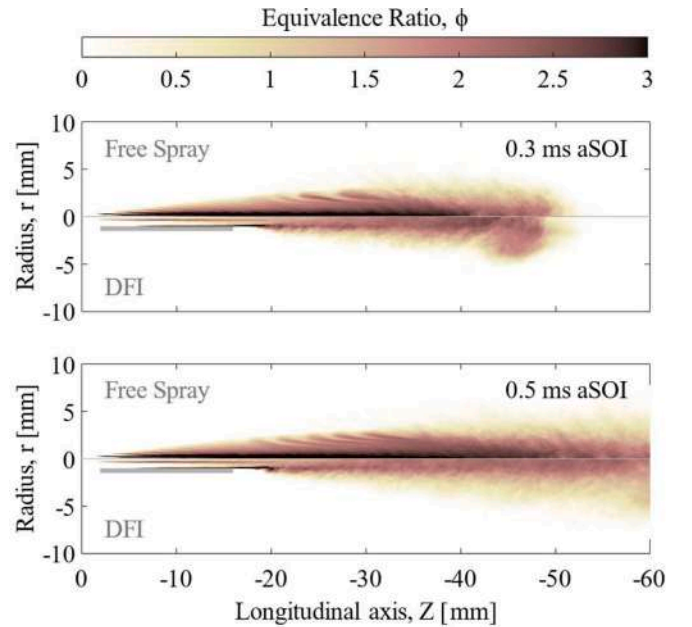
Fig. 9. – Ensemble averaged equivalence ratio field on a semi-slice passing for the spray axis at 0.3 ms aSOI (top) and 0.5 ms aSOI (bottom) for both free spray (top side) and DFI (bottom side).

In order to visualize the turbulent mixing behaviour and better understand the outcome in terms of ϕ, a similar representation is reported in Fig. 10 for the resolved TKE fields.

The energy cascade is spatially more advanced when the duct is adopted, shifting back TKE values higher than 2000 m2/s2 of more than 20 mm. In particular, the transient phase (Fig. 10 - top) highlights that highly turbulent values are localized into the spray tip for the free spray, while they are widely distributed on the whole spray plume for the DFI, leading to a larger and longer area after the duct outlet characterized by high TKE values. This area is then maintained in terms of turbulent intensity and starting location during the injection (Fig. 10 - bottom). Instead, for the free spray, the evolution of the initially formed turbulence into the spray tip leads to a reduction of TKE intensity at constant position.

The enhancement of the turbulent mixing after the duct outlet is caused by the flow detachment at the duct outlet: the spray is suddenly no more guided by the duct wall and strong velocity, density, and concentration gradients appear. This phenomenon triggers the formation of vortices, which remain also within the spray tip during the ducted spray evolution, determining its peculiar shape. This vortices formation was already visible in Fig. 6, where the smallest vortices in the domain were remarkably advanced in terms of space compared to the free spray, manifesting the just mentioned anticipation of the turbulent energy cascade.

It is important to point out that, even though the maximum TKE value in the domain can be higher for the free spray, it is more important that DFI enables a wider and more advanced turbulent mixing, especially considering the limited dimension of a combustion chamber and the necessity to reduce the fuel-to-air ratio before the lift-off length (LOL), which is even extended by the duct adoption (Gehmlich et al., 2018; Mueller et al., 2017).

To get an aggregated and quantitative view of the spray evolution along the axis in terms of TKE and ϕ, their maximum value on the spray cross section was evaluated in previous works (Millo, Piano, Peiretti Paradisi, Segatori, et al., 2021), enabling the comprehension of several DFI working mechanisms. Hence, in Fig. 11, the maximum TKE and ϕ values for each cross-section of the spray at 0.5 ms aSOI are reported as a function of the spray axis for both the free spray and the DFI. To avoid
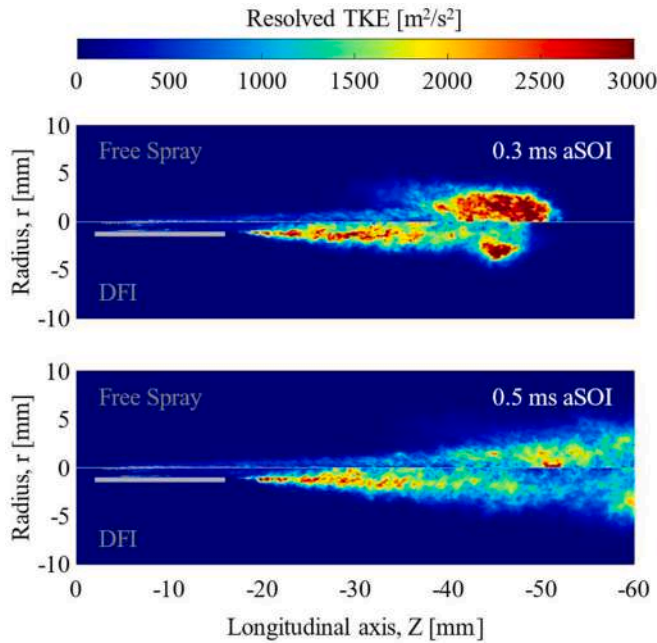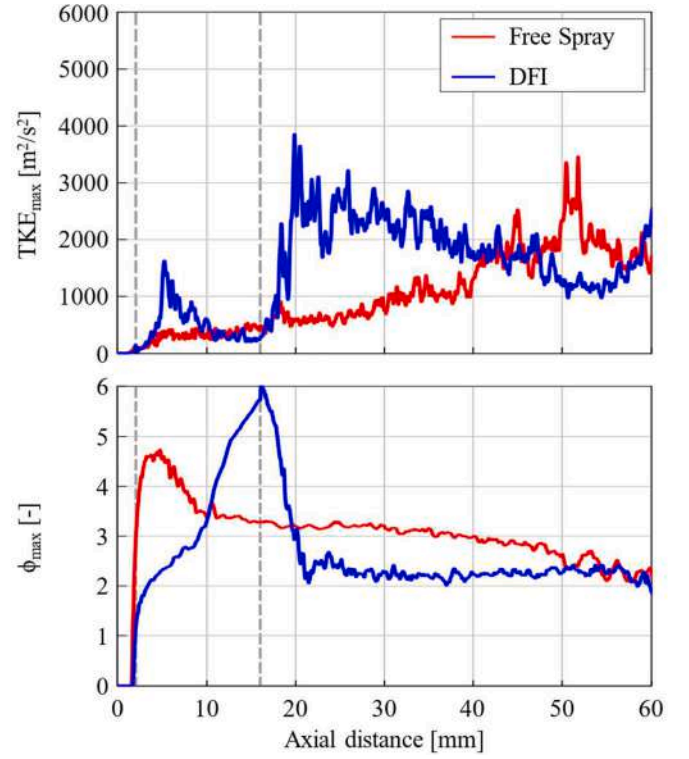

Fig. 11. – Maximum values of the resolved TKE (top) and the equivalence ratio (bottom) on the spray cross section as a function of axial distance at 0.5 ms aSOI according to the ensemble-averaged LES. Results for both free spray (red) and DFI (blue) configurations.

taking into account values which are not statistically converged, axial values were excluded in the computation of the maximum TKE. Indeed, the used runtime saving ensemble average approach, previously discussed, fails close to the spray axis (Farrace et al., 2015), where the semi-slices (assumed as different samples) tend to be statistically dependent for each simulation, due to the very small relative distance, tending to 0 for r = 0 mm. This aspect, for highly fluctuating quantities (e.g., the RMS of the velocity fluctuations to compute the resolved TKE), can prevent the statistical convergence target, which is imperative for this kind of analysis.

The maximum TKE (Fig. 11 - top) behaviour is completely different between free spray (red) and DFI (blue). The former shows an almost linear increment in turbulence when the axial distance increases, while the latter is characterized by two different phases, highlighted by two local peaks. The first turbulence increment occurs inside the duct, few mm after the duct entrance, manifesting a first mixing enhancement related to the duct adoption. The second peak is larger in magnitude and occurs immediately downstream of the duct exit, leading to a second more intense mixing enhancement with respect to the free spray. This confirms and details the DFI working mechanism observed in (Millo, Piano, Peiretti Paradisi, Postrioti, et al., 2021; Millo, Piano, Peiretti Paradisi, Segatori, et al., 2021), defined as two-stage turbulent mixing enhancement. Actually, in this LES study, the turbulent vortices in the ducted-spray tip cause a third positive slope of the DFI curve which can be detected towards the end of the window of interest. In general, a dramatic enhancement of the turbulent mixing is provided by the duct adoption across most of the spray plume.

As a consequence, the free spray and DFI cases show a remarkably different behaviour also in terms of maximum ϕ (Fig. 11 - bottom). At the duct entrance, while the ϕ curves feature a positive slope due to the beginning of fuel evaporation, the slope of the DFI curve reduces its slope due to the 1st stage turbulent mixing enhancement and the pumping effect capable to increase the air entrainment upstream of the

Fig. 10. – Resolved turbulent kinetic energy (TKE) field on a semi-slice passing for the spray axis at 0.3 ms aSOI (top) and 0.5 ms aSOI (bottom) for both free spray (top side) and DFI (bottom side).

duct, dealt with later in the text. Thus, a local ϕ reduction is present for DFI. However, after the liquid spray starts to interact with the duct inner wall, the so-called collision length (Li et al., 2020; Millo, Piano, Peiretti Paradisi, Segatori, et al., 2021) forms, leading to a dramatic ϕ increment close to the duct wall, from which originate the rich pockets observable at the duct exit in Fig. 9. The very fine grid adopted in this study is essential to capture the magnitude of the local ϕ increment. A maximum ϕ equal to 6 is reached for the DFI at the duct exit, which is much higher than the free spray value at equal location. Hence, this effect can explain better the abnormal DFI operation (i.e., much higher soot formation than free spray) observed in the literature (Millo, Segatori, et al., 2021; Mueller et al., 2017; Piano et al., 2022) when the ignition occurs inside the duct (i.e., LOL shorter than the duct exit location). It is noteworthy that more evaporative injection conditions could mitigate the above-described collision length effect, due to reduced liquid/wall interaction. Finally, at the duct exit, the 2nd stage turbulent mixing phenomenon occurs and the DFI curve falls down to maximum ϕ values much lower than the free spray in less than 5 mm. In particular, a maximum ϕ close to 2 is maintained for the ducted-spray whole extension.

To conclude the turbulence comparative analysis, the resolved TKE spectra related to both free spray and DFI configurations in two selected probe locations are reported in Fig. 12. The chosen locations are the duct outlet and half duct length after the duct outlet, namely, where vortices form due to the detachment of the flow. The different radius has been chosen to make the probe staying inside the duct, for the former, and in line with duct wall, for the latter.

At the end of the duct outlet (Fig. 12 - top), it is not evident a turbulence enhancement in the energy containing range (i.e., just developed turbulence) by using the duct. The first part of the inertial subrange presents even slightly higher TKE values for the free spray, while the final part of the resolved spectrum (i.e., smallest turbulent length scales) tends to be slightly higher for the DFI, thus meaning that a higher
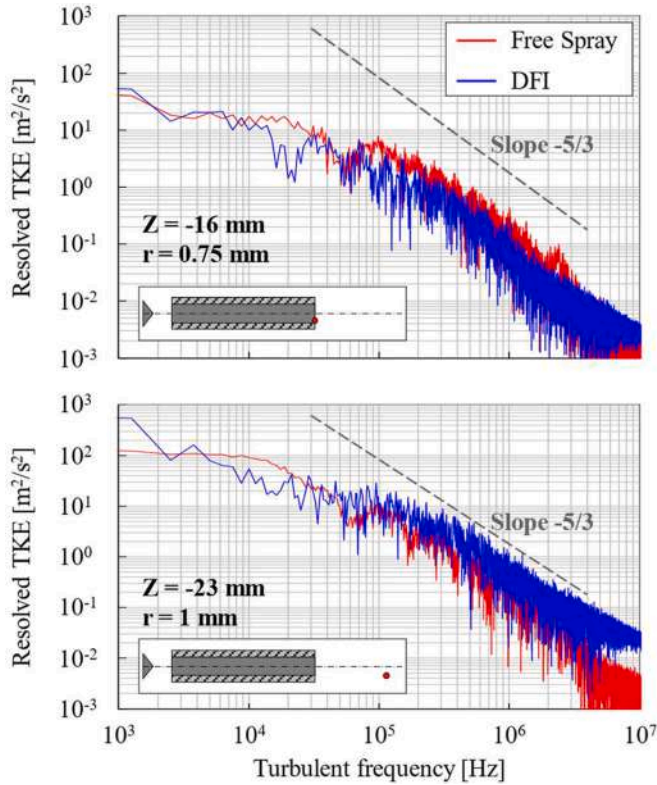
amount of previously formed turbulence is evolving.

Moving downstream of the duct (Fig. 12 – bottom), the DFI spectrum is higher than the free spray one for almost each step of the turbulent energy cascade. This result supports the idea that, after the duct exit, turbulent mixing is enhanced due to vortices which are either just forming because of velocity and density gradients, or evolving according to the energy cascade.

In conclusion, in order to compare each DFI-enabled soot mitigation mechanism detected in the literature, the air entrainment into the fuel spray (Millo, Piano, Peiretti Paradisi, Postrioti, et al., 2021; Nilsen, Yraguen, et al., 2020) was evaluated for both free spray and DFI. In Fig. 13, from top to bottom, the axial velocity, the axial pressure, and the cumulated air entrainment at 0.5 ms aSOI are reported as a function of

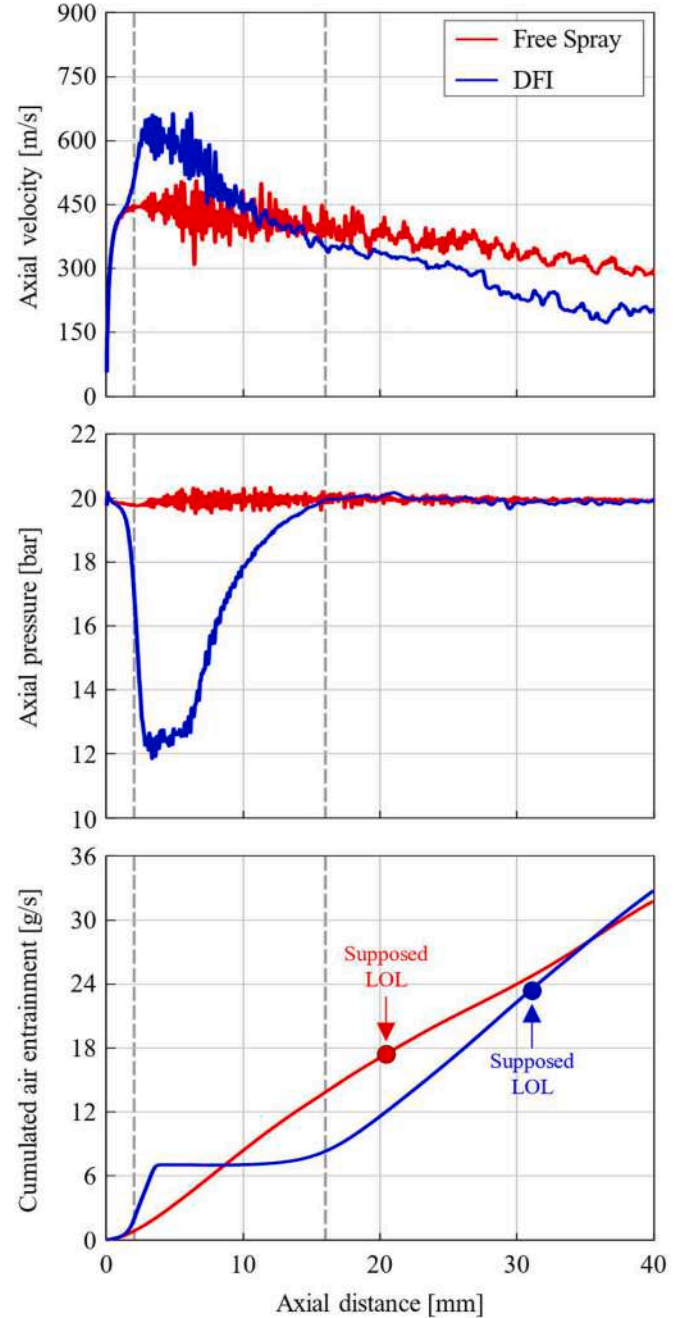**Fig. 13.** – Axial velocity (top), axial pressure (middle), and cumulated air entrainment (bottom) as a function of the axial distance at 0.5 ms aSOI according to the ensemble-averaged LES. Results for both free spray (red) and DFI (blue) configurations.

Fig. 12. – Resolved turbulent kinetic energy (TKE) spectra at selected locations (Z = -16 mm, r = 0.75 mm and Z = -23 mm, r = 1 mm) for both free spray (red) and DFI (blue).

axial distance for both free spray and DFI. The cumulated air entrainment is the air mass flow rate crossing a cone lateral surface, having the vertex at the injector tip (with vertex angle slightly higher than the spray cone angle) and the height equal to the axial distance.

Focusing on the axial velocity (Fig. 13 - top), free spray (red) and DFI (blue) curves diverge close to the duct inlet, due to the spray area restriction provided by the duct presence which results in higher velocities for the DFI spray. Then, a higher momentum transfer between spray and air is observable for DFI by looking at the negative slope of the curves after the peak. This leads to an inversion of the velocity trend between free spray and DFI close to the duct exit. Moving to the axial pressure (Fig. 13 - middle), the difference in the velocity behaviour has consequences in terms of in-duct pressure: a reduction of about 8 bar is detectable, causing the abovementioned pumping effect, whose influence is visible in terms of cumulated air entrainment (Fig. 13 - bottom). In fact, the DFI dramatically enhances the air entrainment upstream of the duct, which is more than doubled with respect to the free spray. Then, after the collision length is established, DFI entrainment remains constant by increasing the axial distance until the flow at the duct exit affects again the surrounding air mass flow rate. Since the free spray behaviour is almost linear throughout the plotting window, the total entrainment immediately downstream of the duct is lower for DFI. However, the first derivative of the DFI curve in this region is higher, thus showing a higher entrainment rate. Therefore, the cumulated air entrainment becomes again equal between the two configurations at about 35 mm axial distance. Therefore, as already concluded in other studies (Piano et al., 2022), the duct presence does not necessarily enhance or reduce the air entrained into the fuel spray from a global point of view, but it changes the entrainment rate distribution across the spray plume, which is enhanced close to the injector. This characteristic can be very beneficial for a successful mixture preparation. Furthermore, considering a combusting case, a longer LOL is expected for the DFI (e.g., the reacting simulations in (Millo, Piano, Peiretti Paradisi, Segatori, et al., 2021) predicted a LOL equal to 21 mm for the free spray and 32 mm for the DFI, indicated by small circles on the plot), leading to a higher air entrainment also from a global point of view.

5. Conclusions

The aim of this work is a comprehensive investigation of ducted fuel injection (DFI) concept in non-reacting conditions through large eddy simulation (LES) turbulence modelling combined with statistical analysis. For this purpose, a 3-dimensional computational fluid dynamics (3D-CFD) spray model, developed in Reynolds-averaged Navier–Stokes (RANS) framework and validated against experimental data in previous works, was employed. A further demonstration of the model reliability is herein provided in terms of predicted liquid spray shape, developing a proper methodology to consistently compare experimental pictures and 3D-CFD simulations (based on the Lagrangian particle tracking approach). The grid settings for this LES analysis were properly examined, highlighting the need for an extremely refined grid for accurate DFI prediction, never achieved so far in the current literature on the subject because of the huge computational cost. Furthermore, the spray/wall interaction model, critical aspect for DFI simulation, was studied from both a results-oriented and scientific literature point of view. Given the scope of employing statistics, 20 samples per each configuration (i. e., free spray and DFI) were considered for the ensemble average process. To curtail the almost prohibitive computational cost, this sample size was obtained by means of only 5 simulations per configuration, adopting a demonstrated runtime saving ensemble average method, exploiting axial symmetry characteristics of the domain. The

investigation was carried out to compare the LES results related to free spray and DFI configurations and, thus, gain further knowledge of DFI working mechanisms in non-reacting conditions. The main outcomes of the herein study can be summarized as follows.

- The run-to-run variability typical of LES is larger when the duct is adopted, manifesting a higher relevance of the turbulence for DFI. It emerges the need for statistical analysis when DFI is investigated through LES.
- The turbulent energy cascade is spatially more advanced when duct is adopted, and the enhanced turbulent mixing areas are generally wider. The anticipation of the mixing is of particular importance considering the limited dimension of a combustion chamber and the necessity to reduce the equivalence ratio before the LOL.
- The spray equivalence ratio distribution is completely modified by the duct adoption in comparison with the standard free spray distribution. The rich central core typical of the free spray configuration is not present, leading to leaner and more homogeneous areas. Rich pockets are present only at the duct exit close to the wall, but they are broken in small lean vortices by the flow detachment and the associated turbulent mixing enhancement occurring downwards the duct exit.
- The DFI soot formation mitigation mechanisms, like air entrainment and turbulent mixing enhancement, previously identified through experiments and RANS analyses, are confirmed by the LES approach. Thanks to its detailed description of the local DFI behaviour, they are significantly improved in quantitative accuracy and understanding.

Future works will assess the possibility to modify the RANS model and improve its outcomes, targeting the herein obtained LES results. If achievable, this approach would result in a low-cost very high-reliability 3D-CFD model.

CRediT authorship contribution statement

C. Segatori: Methodology, Formal analysis, Investigation, Conceptualization, Writing – original draft. **A. Piano:** Conceptualization, Methodology, Investigation, Supervision, Writing – review & editing. **B. Peiretti Paradisi:** Methodology, Investigation, Writing – review & editing. **A. Bianco:** Conceptualization, Methodology. **F. Millo:** Conceptualization, Project administration, Supervision.

Declaration of Competing Interest

The authors declare that they have no known competing financial interests or personal relationships that could have appeared to influence the work reported in this paper.

Data availability

The data that has been used is confidential.

Acknowledgements

Supplementary materials

Supplementary material associated with this article can be found, in the online version, at doi:10.1016/j.ijmultiphaseflow.2023.104686.

Appendix A. DFI spray / wall interaction modelling

According to the results reported in Millo, Piano, Peiretti Paradisi, Postriotssi, et al. (2021), the spray model did not require any variation of the calibration constants to predict both free and DFI sprays. This was deemed as an important outcome of the model validation process and was achieved only if the spray/wall interaction, critical aspect when DFI is concerned (especially in non-reacting weakly evaporative conditions), was described with the rebound/slide model (Gonzalez D. et al., 1991; Naber & Reitz, 1988).

This model, adopted in this work too, enables the drop impacting on the wall to just rebound or slide, according to the normal component of the Weber number, without the formation of a wall film. Although it could seem too simplistic, it could be the most representative option for DFI spray/wall interaction characterization among the models nowadays available. In fact, DFI is a peculiar case due to short distance from injector (thus, high drop velocity at impact) and very low impact angle (i.e., <10–15 deg). In these conditions, typically used wall film models (e.g., O'Rourke & Amsden, 2000;Kuhnke, 2004) led to a not negligible overestimation of splash and thermal breakup phenomena, causing unphysical drop size reduction downstream of the duct, and subsequent liquid penetration degradation. Vice versa, rebound/slide model led to very good penetration prediction and drop size reduction with respect to the free spray, consistent with experimental analysis reported in Millo, Piano, Peiretti Paradisi, Postrioti, et al., 2021. For the sake of completeness, a comparison among the experimental Sauter mean diameter (SMD) reduction provided by the duct adoption and the one predicted by RANS simulations employing the abovementioned spray/wall interaction models (i.e., rebound/slide, O'Rourke, Kuhnke) are reported in Fig. A1. The SMD is evaluated on the spray axis, 50 mm downstream of the injector nozzle. The reference values are related to the models featuring the default coefficients, while the calibration effect refers to the maximum variation of SMD obtained conducting several simulation tests, varying for the DFI configuration the calibration constants of both the spray/wall interaction model and the secondary breakup model through their entire usable range. The parameters of the primary breakup model were kept unchanged since it is strictly related to the injector characteristics, which are unvaried among free spray and DFI.
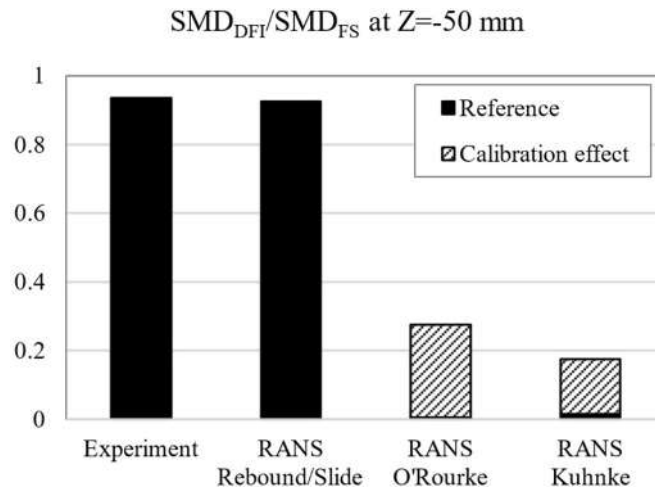
Fig. A1. – DFI Sauter mean diameter (SMD) normalized with respect to the free spray one at Z = -50 mm: comparison among experiments (vessel pressure = 10 bar; vessel temperature = 773 K) and RANS simulations (operating conditions in Table 1) employing different spray/wall interaction models. Filled bar, reference values; patterned bar, maximum effect of spray/wall interaction model and secondary breakup model calibration.

It is evident how the rebound/slide model outperforms the other spray/wall interaction models in the prediction of the SMD variation provided by the duct adoption, even if a calibration effort is considered.

Besides, the absence of a wall film could be physical for the DFI-like conditions, since the possibility of impingement is strongly affected by the dynamic conditions of drop/wall impact, drastically decreasing as the impact angle decreases (Celata et al., 2006; Yao & Cai, 1988) (i.e., droplet motion direction quasi tangential to the wall). As stated, this could be caused by the dramatic reduction of the so-called dynamic Leidenfrost temperature and/or by aerodynamic effects playing a role in preventing drop/wall contact, due to the formation of an interposed gas layer according to the lubrication theory.

Furthermore, an indirect demonstration of the absence of duct wall impingement is provided by Sandia researchers in Mueller et al. (2017). According to their experiments, the luminosity associated with soot incandescence was not detected at the end of the injection, meaning the absence of locally fuel-rich regions related to liquid fuel droplets ripped out of the duct wall by the high-velocity spray. Therefore, "it is believed that liquid fuel did not impinge on the duct wall during injection for any of the studied conditions" (Mueller et al., 2017), partly comparable to the present study in terms of vessel temperature.

In conclusion, the rebound/slide model was deemed as sufficiently motivated from both a practical and physical perspective among the state-of-the-art spray/wall interaction models. It must be specified that this model comes with some drawbacks. In particular, if the droplet dynamics falls in the conditions for a sliding output, the model does not predict any momentum degradation due to friction, leading to a probable overestimation of the velocity close to the duct wall.

Appendix B. Methodology for consistent comparison of experimental optical data and 3D-CFD liquid parcels distribution

It is an open point in the scientific literature to consistently compare the liquid outcome of a Lagrangian 3D-CFD spray (showing all the parcels in

the domain) with the pictures obtained experimentally (e.g., via Schlieren imaging), based on light phenomena (Wang et al., 2021). For this purpose, a methodology was developed to post-process the 3D-CFD parcels distribution, reported in Fig. B1 together with the post-processing procedure adopted for the experimental spray acquisitions.

Among the various techniques (Linne, 2013), the experiments have been postprocessed by binarizing (Tzanetakis et al., 2022) the spray picture to separate the liquid phase by the background colour. Then, the spray perimeter was extracted and reported on a proper reference system and all the aggregated spray quantities of interest (e.g., cone angle, penetration, etc.) can be obtained.

Focusing on the 3D-CFD, a procedure was developed under the hypothesis that the predominant effect of the absence of light in a certain pixel of the experimental spray picture is given by the droplets number density in the pixel itself. In other words, the higher the number of droplets in a certain region, the lower the light intensity. The effect on light intensity caused by other quantities (e.g., droplet diameter, liquid density, etc.) has been considered as of secondary importance. For doing that, firstly, the 3D parcels distribution was projected on a 2-dimensional plane, then, the parcels number density field was computed on a grid featuring the cell size equal to the experimental pixel size. Once this field was available, binarization and spray contour extraction was conducted similarly to experiments.

This method was thus applied to compare the liquid spray outcome obtained through experiments and LES.
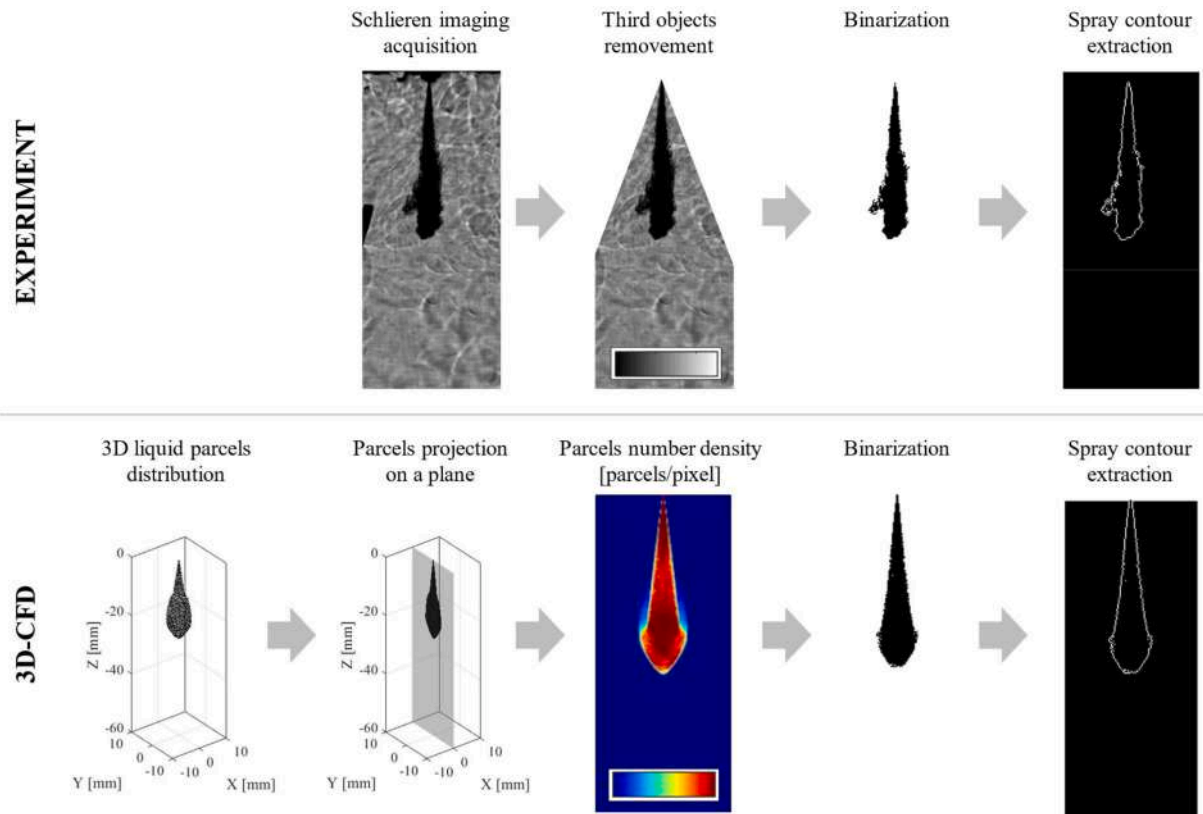
Fig. B1. – Standardized and connected methodologies for the post-processing of the spray liquid data for both experiments applying Schlieren imaging analysis (top) and 3D-CFD simulations applying Lagrangian particle tracking (bottom).

References

ACEA, 2022. New Trucks in the EU by Fuel Type, 2021. Acea. https://www.acea.auto/figure/trucks-eu-fuel-type/.

Amsden, A. A., & Findley, M. (1997). *KIVA-3V: A block-structured KIVA program for engines with vertical or canted valves.*

Amsden, A.A., O'Rourke, P.J., Butler, T.D., 1989. KIVA-II: A computer program for chemically reactive flows with sprays. Los Alamos National Laboratory TechnicalReport LA-11560-MS.

Celata, G.P., Cumo, M., Mariani, A., Zummo, G., 2006. Visualization of the impact of water drops on a hot surface: effect of drop velocity and surface inclination. Heat Mass Transf./Waerme- Und Stoffuebertragung 42 (10), 885–890. https://doi.org/10.1007/s00231-006-0139-1.

Celik, I., Yavuz, I., Smirnov, A., 2001. Large eddy simulations of in-cylinder turbulence for internal combustion engines: a review. Int. J. Engine Res. 2 (2), 119–148. https://doi.org/10.1243/1468087011545389.

Chapman, D.R., 1979. Computational aerodynamics development and outlook. AIAA J. 17 (12), 1293–1313. https://doi.org/10.2514/3.61311.

Chen, T., An, Y., Shen, S., Shi, H., Pei, Y., Wang, K., 2023. Large eddy simulation of fuel-air mixing process in a convergent-divergent duct spray under non-vaporizing conditions. Fuel 353. https://doi.org/10.1016/j.fuel.2023.129176.

Chung, W.T., Ma, P.C., Ihme, M., 2020. Examination of diesel spray combustion in supercritical ambient fluid using large-eddy simulations. Int. J. Engine Res. 21 (1), 122–133. https://doi.org/10.1177/1468087419868388.

Farrace, D., Panier, R., Schmitt, M., Boulouchos, K., Wright, Y.M., 2015. Analysis of averaging methods for large eddy simulations of diesel sprays. SAE Int. J. Fuels Lubric. 8 (3), 568–580. https://doi.org/10.4271/2015-24-2464.

Feng, Y., Shang, T., Cai, J., Sun, K., Wang, T., 2023. Leaner lifted-flame combustion with ducted fuel injection: the key role of forced two-stage mixing. Fuel 347. https://doi.org/10.1016/j.fuel.2023.128431.

Fitzgerald, R.P., Svensson, K., Martin, G., Qi, Y., Koci, C., 2018. Early investigation of ducted fuel injection for reducing soot in mixing-controlled diesel flames. SAE Int. J. Engines 11 (6), 817–833. https://doi.org/10.4271/2018-01-0238.

Gehmlich, R.K., Mueller, C.J., Ruth, D.J., Nilsen, C.W., Skeen, S.A., Manin, J., 2018. Using ducted fuel injection to attenuate or prevent soot formation in mixing-controlled combustion strategies for engine applications. Appl. Energy 226, 1169–1186. https://doi.org/10.1016/j.apenergy.2018.05.078.

Gonzalez, D., , M. A., Borman, G.L., Reitz, R.D, 1991. A study of diesel cold starting using both cycle analysis and multidimensional calculations. SAE Trans., pp. 189–208.

Guo, J., Brouzet, D., Chung, W.T., Ihme, M., 2023. Analysis of ducted fuel injection at high-pressure transcritical conditions using large-eddy simulations. Int. J. Engine Res., 146808742311706 https://doi.org/10.1177/14680874231170659.

Hanjalic, K., 2005. Will RANS survive LES? A view of perspectives. J. Fluids Eng. Trans. ASME 127 (5), 831–839. https://doi.org/10.1115/1.2037084.

Heywood, J.B., 1988. Internal Combustion Engine Fundamentals. McGraw-Hill, New York.

Hu, B., Banerjee, S., Liu, K., Rajamohan, D., Deur, J.M., Xue, Q., Som, S., Senecal, P.K., Pomraning, E., 2015. Large eddy simulation of a turbulent non-reacting spray jet. In:

ASME 2015 Internal Combustion Engine Division Fall Technical Conference, ICEF 2015, 2. https://doi.org/10.1115/ICEF2015-1033.

IEA International Energy Agency, 2022. World Energy Outlook 2022.

Issa, R.I., 1986. Solution of the implicitly discretised fluid flow equations by operator-splitting. J. Comput. Phys. 62 (1), 40–65. https://doi.org/10.1016/0021-9991(86)90099-9.

Kuhnke, D. (2004). *Spray/Wall-interaction Modelling by Dimensionless Data Analysis* (S. Verlag, Ed.).

Li, F., Lee, C.fon, Wang, Z., Liu, F., Lu, G, 2020. Optical investigation on impacts of ambient pressure on macroscopic spray characteristics of ducted fuel injection under non-vaporizing conditions. Fuel 268, 117192. https://doi.org/10.1016/j.fuel.2020.117192.

Li, F., Lee, C.fon, Wu, H., Wang, Z., Liu, F, 2019. An optical investigation on spray macroscopic characteristics of ducted fuel injection. Experim. Therm. Fluid Sci. 109, 109918 https://doi.org/10.1016/j.expthermflusci.2019.109918.

Linne, M., 2013. Imaging in the optically dense regions of a spray: A review of developing techniques. Progr. Energy Combus. Sci. 39 (5), 403–440. https://doi.org/10.1016/j.pecs.2013.06.001.

Liu, A.B., Mather, D., Reitz, R.D., 1993. Modeling the effects of drop drag and breakup on fuel sprays. SAE Tech. Paper 930072. https://doi.org/10.4271/930072.

Lucchini, T., Zhou, Q., D'Errico, G., Severgnini, D, 2022. Modeling fuel-air mixing, combustion and soot formation with ducted fuel injection using tabulated kinetics. *SAE Tech. Papers, 2022.* https://doi.org/10.4271/2022-01-0403.

Martínez, J., Piscaglia, F., Montorfano, A., Onorati, A., Aithal, S.M., 2015. Influence of spatial discretization schemes on accuracy of explicit LES: Canonical problems to engine-like geometries. Comp. Fluids 117, 62–78. https://doi.org/10.1016/j.compfluid.2015.05.007.

Mathworks. (2021). *MATLAB, Release 2021a.*

Millo, F., Piano, A., Peiretti Paradisi, B., Postrioti, L., Pieracci, L., Bianco, A., Pesce, F.C., Vassallo, A., 2021. Ducted fuel injection: experimental and numerical investigation on fuel spray characteristics, air/fuel mixing and soot mitigation potential. Fuel 289, 119835. https://doi.org/10.1016/j.fuel.2020.119835.

Millo, F., Piano, A., Peiretti Paradisi, B., Segatori, C., Postrioti, L., Pieracci, L., Bianco, A., Pesce, F.C., Vassallo, A., 2021. Ducted fuel injection: a numerical soot-targeted duct geometry optimization. SAE Int. J. Engines 15 (2). https://doi.org/10.4271/03-15-02-0014.

Millo, F., Segatori, C., Piano, A., Peiretti Paradisi, B., Bianco, A., 2021. An engine parameters sensitivity analysis on ducted fuel injection in constant-volume vessel using numerical modeling. SAE Technical Paper. https://doi.org/10.4271/2021-24-0015, 2021-24-0015.

Mockett, C., Fuchs, M., Thiele, F., 2012. Progress in DES for wall-modelled LES of complex internal flows. Comp. Fluids 65, 44–55. https://doi.org/10.1016/j.compfluid.2012.03.014.

Mockett, C., Thiele, F., 2007. Overview of detached-eddy simulation for external and internal turbulent flow applications. New Trends Fluid Mech. Res. 79–82. https://doi.org/10.1007/978-3-540-75995-9_20.

Mueller, C.J., Nilsen, C.W., Ruth, D.J., Gehmlich, R.K., Pickett, L.M., Skeen, S.A., 2017. Ducted fuel injection: A new approach for lowering soot emissions from direct-injection engines. Appl. Energy 204, 206–220. https://doi.org/10.1016/j.apenergy.2017.07.001.

Naber, J.D., Reitz, R.D., 1988. Modeling Engine Spray/Wall Impingement. SAE Tech. Paper 880107. https://doi.org/10.4271/880107.

Nilsen, C.W., Biles, D.E., Mueller, C.J., 2019. Using ducted fuel injection to attenuate soot formation in a mixing-controlled compression ignition engine. SAE Int. J. Engines 12 (3), 309–322. https://doi.org/10.4271/03-12-03-0021.

Nilsen, C.W., Biles, D.E., Yraguen, B.F., Mueller, C.J., 2020. Ducted fuel injection versus conventional diesel combustion: an operating-parameter sensitivity study conducted in an optical engine with a four-orifice fuel injector. SAE Int. J. Engines 13 (3). https://doi.org/10.4271/03-13-03-0023.

Nilsen, C.W., Yraguen, B.F., Mueller, C.J., Genzale, C., Delplanque, J.-P., 2020. Ducted fuel injection vs. free-spray injection: a study of mixing and entrainment effects using numerical modeling. SAE Int. J. Engines 13 (5). https://doi.org/10.4271/03-13-05-0044.

Nyrenstedt, G., Nilsen, C.W., Biles, D.E., Mueller, C.J., 2023. Ducted fuel injection with low-net-carbon fuels as a solution for meeting future emissions regulations. Fuel 338. https://doi.org/10.1016/j.fuel.2022.127167.

Ong, J.C., Zhang, M., Jensen, M.S., Walther, J.H., 2022. Large eddy simulation of soot formation in a ducted fuel injection configuration. Fuel 313. https://doi.org/10.1016/j.fuel.2021.122735.

O'Rourke, P.J., Amsden, A.A., 2000. A spray/wall interaction submodel for the KIVA-3 wall film model. SAE Tech. Papers. https://doi.org/10.4271/2000-01-0271.

Piano, A., Segatori, C., Millo, F., Pesce, F.C., Vassallo, A.L., 2022. Investigation of ducted fuel injection implementation in a retrofitted light-duty diesel engine through numerical simulation. SAE Int. J. Engines 16 (5). https://doi.org/10.4271/03-16-05-0038, 03-16-05-0038.

Pierpont, D.A., Montgomery, D.T., Reitz, R.D., 1995. Reducing particulate and nox using multiple injections and egr in a D.I. diesel. SAE Tech. Papers. https://doi.org/10.4271/950217.

Piomelli, U., 2008. Wall-layer models for large-eddy simulations. Progr. Aerospace Sci. 44 (6), 437–446. https://doi.org/10.1016/j.paerosci.2008.06.001.

Pitsch, H., Steiner, H., 2000. Large-eddy simulation of a turbulent piloted methane/air diffusion flame (Sandia flame D). Phys. Fluids 12 (10), 2541–2554. https://doi.org/10.1063/1.1288493.

Polonowski, C.J., Mueller, C.J., Gehrke, C.R., Bazyn, T., Martin, G.C., Lillo, P.M., 2012. An experimental investigation of low-soot and soot-free combustion strategies in a heavy-duty, single-cylinder, direct-injection, optical diesel engine. SAE Int. J. Fuels Lubric. 5 (1), 51–77. https://doi.org/10.4271/2011-01-1812.

Pomraning, E., Rutland, C.J., 2002. Dynamic one-equation nonviscosity large-eddy simulation model. AIAA J.l 40 (4), 689–701. https://doi.org/10.2514/2.1701.

Pope, S.B., 2000. Turbulent Flows. Cambridge University Press.

Pope, S.B., 2004. Ten questions concerning the large-eddy simulation of turbulent flows. New J. Phys. 6 https://doi.org/10.1088/1367-2630/6/1/035.

Reitz, R.D., Bracco, F.V., 1986. Mechanisms of breakup of round liquid jets. Encyclop. Fluid Mech. 3.

Reitz, R.D., Diwakar, R., 1987. Structure of high-pressure fuel sprays. SAE Tech. Paper 870598. https://doi.org/10.4271/870598.

Rhie, C.M., Chow, W.L., 1983. Numerical study of the turbulent flow past an airfoil with trailing edge separation. AIAA J. 21 (11), 1525–1532. https://doi.org/10.2514/3.8284.

Richards, K. J., Senecal, P. K., & Pomraning, E. (2022). *CONVERGE 3.0.14.*

Segatori, C., Piano, A., Peiretti Paradisi, B., Millo, F., Bianco, A., 2023. Ensemble average method for runtime saving in large eddy simulation of free and ducted fuel injection (DFI) sprays. Fuel. https://doi.org/10.1016/j.fuel.2023.128110.

Senecal, P.K., Pomraning, E., Richards, K.J., Som, S., 2013. An investigation of grid convergence for spray simulations using an les turbulence model. SAE Tech. Papers 2. https://doi.org/10.4271/2013-01-1083.

Senecal, P.K., Pomraning, E., Richards, K.J., Som, S., 2014. Grid-Convergent Spray Models for Internal Combustion Engine Computational Fluid Dynamics Simulations. J. Energy Resour. Technol. 136 (1) https://doi.org/10.1115/1.4024861.

Senecal, P.K., Pomraning, E., Xue, Q., Som, S., Banerjee, S., Hu, B., Liu, K., Deur, J.M., 2014. Large eddy simulation of vaporizing sprays considering multi-injection averaging and grid-convergent mesh resolution. J. Eng. Gas Turbines Power 136 (11). https://doi.org/10.1115/1.4027449.

Senecal, P. K., Richards, K. J., Pomraning, E., Yang, T., Dai, M. Z., McDavid, R. M., Patterson, M. A., Hou, S., & Shethaji, T. (2007). *A new parallel cut-cell Cartesian CFD code for rapid grid generation applied to in-cylinder Diesel engine simulations.*

Skeen, S.A., Manin, J., Pickett, L.M., Cenker, E., Bruneaux, G., Kondo, K., Aizawa, T., Westlye, F., Dalen, K., Ivarsson, A., Xuan, T., Garcia-Oliver, J.M., Pei, Y., Som, S., Hu, W., Reitz, R.D., Lucchini, T., D'Errico, G., Farrace, D., Hawkes, E., 2016. A progress review on soot experiments and modeling in the engine combustion network (ECN). SAE Int. J. Engines 9 (2). https://doi.org/10.4271/2016-01-0734, 2016-01-0734.

Slimon, S., 2003. Computation of internal separated flows using a zonal detached eddy simulation approach. Am. Soc. Mech. Eng. Fluids Eng. Division (Publication) FED 259, 423–433. https://doi.org/10.1115/IMECE2003-43881.

Spalart, P.R., 2009. Detached-eddy simulation. Ann. Rev. Fluid Mech. 41 (May), 181–202. https://doi.org/10.1146/annurev.fluid.010908.165130.

Speziale, C.G., 1997. Turbulence modeling for time-dependent rans and vles: a review. In: 13th Computational Fluid Dynamics Conference, pp. 1071–1090. https://doi.org/10.2514/3.13796.

Svensson, K.I., Martin, G.C., 2019. Ducted fuel injection: effects of stand-off distance and duct length on soot reduction. SAE Int. J. Adv. Curr. Prac. Mobility 1 (3), 1074–1083. https://doi.org/10.4271/2019-01-0545, 1074–1083.

Travin, A.K., Shur, M.L., Spalart, P.R., Strelets, M.K., 2006. Improvement of delayed detached-eddy simulation for LES with wall modelling. Proc. Eur. Conf. Comp. Fluid Dyn. (ECCOMAS CFD 2006) 47 (2), 345–360.

Tzanetakis, T., Johnson, J., Schmidt, H., Atkinson, W., Naber, J., 2022. Non-reacting spray characteristics of gasoline and diesel with a heavy-duty single-hole injector. Front. Mech. Eng. 8 https://doi.org/10.3389/fmech.2022.887657.

Villafuerte, P. M. (2022). *AECC-IPA ultra-low emissions heavy-duty demo vehicle – data analysis in view of Euro 7.* https://www.aecc.eu/event/aecc-ipa-euro-7-technical-seminar-and-driving-event/.

Wang, S., Cao, J., Yang, S., Li, X., Hung, D.L.S., Xu, M., 2021. Post processing method for lagrangian spray field based on mie scattering theory. Int. Conf. Liquid Atomiz. Spray Syst. (ICLASS) 1 (1). https://doi.org/10.2218/iclass.2021.6077.

Werner, H., Wengle, H. (1991). *Large eddy simulation of turbulent flow over and around a cube in plane channel.* 155–168.

Yao, S.C., Cai, K.Y., 1988. The dynamics and leidenfrost temperature of drops impacting on a hot surface at small angles. Experim. Therm. Fluid Sci. 1 (4), 363–371. https://doi.org/10.1016/0894-1777(88)90016-7.

Zhang, Y., Wang, Z., Lee, C.fon, Li, F., Wu, H, 2021. Analysis of mechanism of ducted fuel injection under non-vaporizing condition. Fuel 305. https://doi.org/10.1016/j.fuel.2021.121496.

Zhou, T., Roorda, M.J., MacLean, H.L., Luk, J., 2017. Life cycle GHG emissions and lifetime costs of medium-duty diesel and battery electric trucks in Toronto, Canada. Transp. Res. Part D Transp. Environ. 55, 91–98. https://doi.org/10.1016/j.trd.2017.06.019.